Radiation Measurements 176 (2024) 107212

Contents lists available at ScienceDirect

Radiation Measurements

journal homepage: www.elsevier.com/locate/radmeas

Two-dimensional real-time dosimetry system using micro-and nano-$(C_{44}H_{38}P_2)MnCl_4$ radioluminescence coatings

Luana de Freitas Nascimento [a,*], Marijke De Saint-Hubert [a], Wouter Crijns [b], Marco Caprioli [b], Laurence Delombaerde [b], Dirk Vandenbroucke [c], Paul Leblans [c], Paul Sterckx [c], Katleen Himschoot [c], Jo Goossens [d], Verdi Vanreusel [d], Dirk Verellen [d]

[a] Belgian Nuclear Research Centre, Research in Dosimetric Applications, Mol, Belgium
[b] Department of Radiation Oncology, Leuvens Kankerinstituut, Leuven, Belgium
[c] AGFA NV, Mortsel, Belgium
[d] Iridium Kankernetwerk, University of Antwerp, Antwerp, Belgium

A B S T R A C T

This study investigates the impact of particle size on the radioluminescence (RL) response of $(C_{44}H_{38}P_2)MnCl_4$ coatings, which have been made with five crystal size fractions ranging from ≈200 nm to 75 μm. These coatings underwent testing using a bespoke 2D real time prototype system, comprising a camera affixed to the head of a linear accelerator and oriented towards the flexible RL coatings positioned at the beams' isocentre. Upon irradiation, a consistent RL peak at 525 nm was observed across all particle size fractions, albeit with varying light intensities. Minimum detectable dose-rate values were determined to be 0.05 Gy/min, and even for the coating exhibiting the lowest light intensity (Nano-01), individual pulses could be discerned, yielding a minimum detectable dose of 0.28 mGy. Basic dosimetric tests were conducted to characterize these coatings, evaluating their response with respect to dose-rate, dose, and small field relative responses. Subsequently, the coating demonstrating the most favorable dosimetric properties underwent further analysis to assess its suitability for machine quality assurance (QA). These tests included the standard alternating leaves, chair, and pyramid checks routinely employed for QA purposes.

1. Introduction

There is a continual need for more accurate and effective dosimetric systems for machine quality assurance (QA) and patient specific quality assurance (PSQA) as radiotherapy evolves in complexity. Ideally, these verifications should include the direct dose measurement for every beam, every fraction, and for every patient. There are numerous solutions to verify the pre-treatment delivery to a phantom (Bresciani et al., 2018; Rangaraj et al., 2019). However, pre-treatment QA is the least sensitive tool to detect errors out of all control checks in radiation oncology (Mijnheer, 2019; Stevens et al., 2023), highlighting the need for real-time dosimetric systems.

Scintillators have been vastly studied as candidates for effective real-time dosimetry in radiotherapy (Beddar and Beaulieu, 2016). Inorganic scintillators are typically classified into two categories - single-crystals and polycrystalline ceramics; with the former typically exhibiting better optical properties at the expense of fabrication costs. However, they have limited application in external radiotherapy due to their high effective atomic number (Z_{eff}), that directly impact their energy dependence. Organic scintillators are sub-divided into plastic and liquid scintillators. Their main advantage is tissue equivalency (TE) due to Zeff close to water (Beaulieu and Beddar, 2016). A new class of organic–inorganic hybrid metal halides have emerged as promising materials for scintillation applications due to high photoluminescence quantum yield (PQY) and low cost. In particular, the Tetrabutylammonium(TBA) CuX_2 (X = Cl, Br) (Lian et al., 2021), $(C_{38}H_{34}P_2)MnBr_4$ (Xu et al., 2020), $(C_8H_{20}N)_2MnBr_4$ (Jiang et al., 2021) and $(C_{40}H_{38}P_2)MnBr_4$ (Xu et al., 2022) hybrids exhibit promising detection performances.

Crystal size is one important parameter on the composition of such organic–inorganic hybrid detectors, as it plays a critical role in optimizing their dosimeter performance for reasons including energy dependence, efficiency of converting absorbed radiation into light, spatial resolution and signal-to-noise ratio. Several studies have investigated the effect of particle size in the response of dosimetric materials in various radiation types (Aboelezz and Pogue, 2023; Bhadane et al., 2020; de Freitas Nascimento et al., 2022; De Saint-Hubert et al., 2024a; Pagonis et al., 2023). Ideally, a dosimeter should exhibit minimal variation in response across the range of radiation energies encountered in radiotherapy. Organic–inorganic hybrid composites with larger inorganic scintillators crystals, have a higher Z_{eff}, i.e. are non TE. The

* Corresponding author.
E-mail address: ldfnasci@sckcen.be (L. de Freitas Nascimento).

https://doi.org/10.1016/j.radmeas.2024.107212
Received 29 February 2024; Received in revised form 11 June 2024; Accepted 20 June 2024
Available online 21 June 2024

Table 1
Overview of coatings.

Coating name	Crystal size (μm), D50	Phosphor	Decay time (ms)	Active thickness (μm) and area (mm^2)	Peak emission (nm)
Nano-01	0.2	$(C_{44}H_{38}P_2)MnCl_4$	5.0	45 and 150 × 150	525
Micro-01	3			75 and 150 × 150	
Micro-02	7			75 and 150 × 150	
Micro-03	12			95 and 150 × 150	
Micro-04	75			123 and 150 × 150	
Al_2O_3	7	Al_2O_3:C, Mg (Rodriguez et al., 2011)	35.0	100 and 150 × 150	420

presence of higher Z_{eff} enhances the probability of photoelectric interactions at low photon energies (<100 keV), resulting in over-response doses when compared to water (Attix, 2008).

Several of these RL/scintillators materials have been coupled to plastic or silica optical fibres (Beaulieu and Beddar, 2016; de Freitas Nascimento et al., 2022; Nascimento et al., 2018; Veronese et al., 2010). These point detectors present several advantages, such as high spatial resolution, stability, flexibility, low cost, real time measurement and potential for small field dosimetry applications. In addition to the ever-growing scientific literature on this subject, scintillator devices are also becoming commercially available (Galavis et al., 2019; Timakova et al., 2023).

Attempts to design multidimensional (1D, 2D and 3D) real time systems included using multiple single-probe arrays, packed closely together (Guillot et al., 2011; O'Keeffe et al., 2015) and more recent alternatives using cameras (Jenkins et al., 2015; Nascimento et al., 2020, 2021). When looking for in vivo dosimetry (IVD) and PSQA, the use of multiplexed fibres to compose a matrix becomes complex while camera sensors placed on the head of a linear accelerator, or tripod, facing these coatings are capable to visualize the position, shape, and intensity of the radiation beam as it reaches the coating. The camera setup can be used for IVD, for transmission dosimetry, for creating transit images and for patient and machine QA. Patient treatment plans are modulated using MultiLeaf Collimators (MLC) that dynamically shape the geometry of the primary beam, while partially shielding it. That modifies the nominal spectrum of the primary beam, shifting it towards lower energies according to treatment-specific beam modulation (e.g., static, dynamic, intensity-modulated radiotherapy, volumetric modulated arc therapy). A way to reduce energy dependence in scintillators, as mentioned above, consists of decreasing the size of particles in composites, while controlling the particle load.

The purpose of this work was to present an improvement to our previous works (Nascimento et al., 2020, 2021), initially based on Al_2O_3:C and Al_2O_3:C,Mg coatings; by introducing new coatings that minimally perturbs the main beam, while assessing its real time 2D dose-rate. This work is part of the "Quality Assurance in RadioTherapy by Stimulated and Excited Luminescence Dosimetry - QUARTEL" project (funded by the Flanders Innovation and Entrepreneurship-VLAIO, Belgium), where one of the goals was to develop TE dosimetric solutions based on luminescence materials. To reach this goal, we studied new $(C_{44}H_{38}P_2)MnCl_4$-based coatings made with different crystal sizes (micro to nano) and its suitability as a radiation detection technology that can be applied to surface dose estimation and machine QA. We present the dosimetric characterization and proof of concept of our system in external beam radiotherapy, and demonstrate the impact of crystal sizes in respect to relative dose response in various field sizes.

2. Materials and methods

2.1. Coatings and system setup

The coatings based on micro-and nano-$(C_{44}H_{38}P_2)MnCl_4$ are described in Table 1. We tested five types of coatings produced by AGFA NV (Belgium), in comparison to the Al_2O_3:C; Mg coating used in our previous work (Nascimento et al., 2021). Both Al_2O_3:C; Mg and Al_2O_3:C are well stablished radiophotoluminescence (RPL) (Akselrod and Akselrod, 2006) and optically stimulated luminescence (OSL) materials (Yukihara et al., 2014), respectively. The active layer of the coatings, with average density of 1.15 g/cm^3, consisted of the $(C_{44}H_{38}P_2)MnCl_4$ particles dispersed in a binder, composed by a combination of hydrogenated styrenic block copolymers (Kraton, USA) and polydimethylsiloxane silicon (named Baysilone), deposited on a near-water equivalent substrate of a white opaque polyester-based synthetic paper with thickness of 115 μm (Synaps 115, AGFA NV (AGFA, 2024). The phosphor concentration was 15% for all coatings and the mean particle size of the phosphors, presented in Table 1, represents D50, i.e. mass-median diameter, where the particle size at which 50% of the material (by mass) is smaller than that size and the remaining 50% is larger. The standard deviation of particle size is ≈ 10%. The indicated decay time and emission were measured using a Fluorolog-3 spectrofluorometer (model FL3-22, Horiba Jobin Yvon Inc.). The emission monochromator was scanned from 300 to 850 nm in 1 nm steps.

The luminescence acquisition system consisted of an Complementary Metal-Oxide-Semiconductor (CMOS) camera (Basler) that replaced the Electron Multiplying Charge Coupled Device (EMCCD) camera (Raptor photonics) used in our previous works (Nascimento et al., 2020, 2021, 2022), because this EMCCD camera has been discontinued in the recent years. The CMOS camera (4512 pixels × 4512 pixels, 20.2 MP, Sony IMX541 sensor) combined with an optical lens was fixed in the head of the linear accelerator (LINAC), focused on the field isocentre at an angle

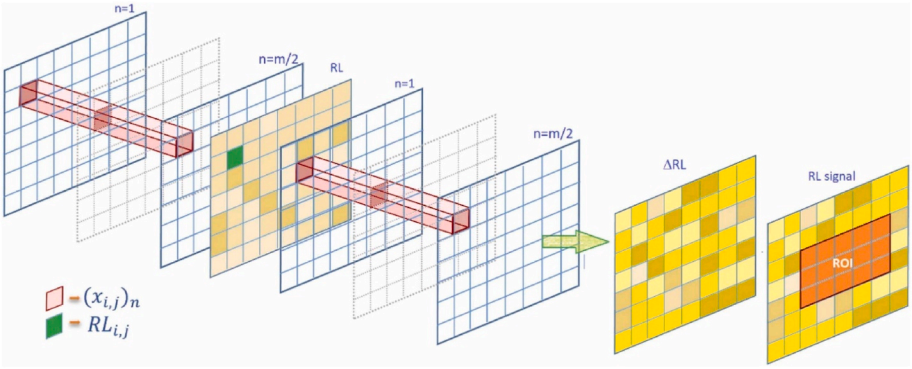

Fig. 1. Representation of the 'RL signal' as the average of ΔRL (RL-Bkgd) pixels over a ROI.

Fig. 2. Camera placed at the head of the LINAC, facing the beam's isocentre.

of ~45° and distance of 100 cm (Fig. 2), and was controlled by the Basler-Pylon dedicated software (Basler, 2024). For all measurements presented in this work, with exception of the afterglow test, we used a frame rate of 20 ms and an Electron Multiplying Gain (EM gain) of 20 dB.

To translate the measured images into meaningful dosimetric quantities, firstly, the raw images were corrected for angular distortion. This distortion was due to the camera's angle relative to the irradiated field. To rectify this, the "Interactive Perspective" plugin from Fiji software was employed (Schindelin et al., 2012). This plugin corrects for angular distortions, using a set of corresponding points between the distorted image and a reference image with a known, undistorted geometry.

Secondly, each pixel within the raw image represented a specific area on the detector. This created a calibrated space where pixel values directly corresponded to a known area on the detector. Essentially, the methodology involved using known CMOS sensor characteristics (pixel size, number of pixels, field of view), camera positioning (angle and distance), and geometric relationships to establish a calibration that represents a specific real-world area (0.1 × 0.1 mm^2 in this case) to each pixel in the captured image. This allows us to convert raw pixel values into meaningful units.

Thirdly, high-energy scattered particles saturated certain pixels, introducing noise into the image. To address this issue, a Wiener noise removal filter was applied to affected areas. This filter smooths out the noise while preserving the underlying signal, ensuring a cleaner and more accurate representation of the data.

Finally, background signal unrelated to radiation was isolated from the signal caused by radiation. This involved subtracting the average background signal ($\overline{Bkgd}_{i,j}$) from each pixel value ($RL_{i,j}$) over a specified region of interest (ROI). The difference obtained is denoted by $\Delta RL_{i,j}$, often referred to as "Delta RL" for convenience, which represents dose-rate. Each background image was acquired by averaging, pixel by pixel, 25 images prior and 25 images post irradiation (m = 50, Fig. 1). The standard deviation (SD) divided by the average of the background light did not exceed ≈0.5 % for the $(C_{44}H_{38}P_2)MnCl_4$ coatings. The integrated $\Delta RL_{i,j}$ signal in time ($\sum_t \Delta RL_{i,j} * t$) is proportional to the dose and is referred as "integrated Delta RL" (Fig. 1, equation (1)). For more details, we refer to our previous works (Nascimento et al., 2020, 2021, 2022).

$$\left\{ \begin{array}{l} \Delta RL_{i,j} = RL_{i,j} - \overline{Bkgd}_{i,j} \\ \Delta RL_{i,j} = RL_{i,j} - \left[\frac{1}{m} * \sum_{n=1}^{m} (x_{i,j})_n \right] \\ \text{'RL signal'} = \Delta \overline{RL}_{i,j\ ROI} \end{array} \right\} \quad \text{equation 1}$$

In essence, the transformation process takes raw pixel data and corrects for distortions, assigns a physical meaning to each pixel value (area), addresses potential noise issues, and isolates the radiation-induced signal for dosimetric analysis.

2.2. Irradiations and tests

We irradiated the coatings using a Varian TrueBeam linear accelerator (Varian Medical Systems Inc., Palo Alto, CA) with 6 MV photons in both flattening filter (FF) and flattening filter free (FFF) modes. Reference data for dose and relative intensities vs field sizes were obtained using ionization chambers and radiochromic films Gafchromic™ EBT3 (Borca et al., 2013). The LINAC was calibrated using the NCS report 18 (Stralingsdosimetrie, 2008) to obtain an equivalence of 1 cGy/1 MU at depth of maximum dose (d_{max}) in reference conditions, for a 100 × 100 mm^2 field size and a 100 cm source-to-surface distance (SSD). For 6 MV, d_{max} = 16 mm for FF and 18 mm for FFF.

The decision tree on selecting the most suitable candidate for surface dosimetry and QA followed the sequence below:

First, we investigated if the film interfered with the radiation beam. We placed it at the surface of a slab phantom and measured dose (100 MU) versus depth using an optical fibre prototype (Nascimento et al., 2015, 2018). We then compared these results with those obtained when the coatings were not present in the 100 × 100 mm^2 beam path. The fibre was positioned at both the centre of the field (x = 0) and an out-of-field location (x = 60 mm). The "AAPM's TG-51 protocol for clinical reference dosimetry of high-energy photon and electron beams" (Almond et al., 1999) acknowledges the impact of beam hardening and offers recommendations for minimizing its influence on dosimetry, however, it doesn't provide a specific "acceptable" level. For this test, we used the acceptance criteria of ±3% (one standard deviation) for dose assessment in conventional field sizes used in radiotherapy, according to common recommendations and practices (Andreo et al., 2002; Huq et al., 2001).

Afterglow was measured using normalized RL counts (relative to the maximum signal) from a $(C_{44}H_{38}P_2)MnCl_4$ (Micro-01) coating and the

Table 2
Difference of measured dose at difference depths in a 100 × 100 mm^2, 6 MV FF beam where the point optical fibre system is placed at the isocentre of the beam (x = 0 mm), with and without the coatings.

Depth	Fibre dose without coating	Nano-01	Micro-01	Micro-02	Micro-03	Micro-04	Al_2O_3
6 MV FF							
mm	Gy	Difference (%)					
16	1.000 ± 0.001	−0.1	−0.2	−0.2	−0.5	−0.5	−0.4
25	0.967 ± 0.001	−0.2	−0.3	−0.3	−0.5	−0.5	−0.3
30	0.945 ± 0.001	−0.2	−0.3	−0.2	−0.5	−0.6	−0.4
50	0.861 ± 0.001	−0.3	−0.3	−0.3	−0.5	−0.6	−0.4
70	0.778 ± 0.001	−0.3	−0.4	−0.3	−0.6	−0.7	−0.4
100	0.664 ± 0.001	−0.3	−0.3	−0.4	−0.7	−1.0	−0.4
Depth	Fibre dose without coating	Nano-01	Micro-01	Micro-02	Micro-03	Micro-04	Al_2O_3
6 MV FFF							
mm	Gy	Difference (%)					
18	1.000 ± 0.001	−0.3	−0.4	−0.3	−0.6	−0.6	−0.6
25	0.960 ± 0.001	−0.3	−0.3	−0.3	−0.5	−0.7	−0.4
30	0.940 ± 0.001	−0.4	−0.3	−0.4	−0.6	−0.6	−0.5
50	0.850 ± 0.001	−0.3	−0.4	−0.3	−0.5	−0.7	−0.6
70	0.761 ± 0.001	−0.4	−0.4	−0.4	−0.5	−0.8	−0.7
100	0.639 ± 0.001	−0.4	−0.5	−0.4	−0.6	−0.9	−0.8

Al_2O_3:C; Mg coating placed on the surface of a slab phantom. The coatings were irradiated for 10 s with a 600 MU/min dose rate in FF mode at a SSD of 100 cm and a field size of 100 × 100 mm^2. Following beam shutoff, the signal from the coatings was recorded at 120 frames per second (fps). The acceptance criterion was that the $(C_{44}H_{38}P_2)MnCl_4$ coating should not exhibit afterglow, meaning the background signal before and after irradiation should not vary beyond the system's accuracy.

For the dosimetric characterization, we performed dose-rate/dose response and field size dependence measurements for various field sizes. The dose-rate response was investigated by irradiating coatings at surface with dose rates ranging from 5 to 600 (FF) monitor units per minute (MU/min) and from 400 to 1400 MU/min (FFF), field size of 100 × 100 mm^2, SSD of 100 cm. We used the acceptance criteria of ±2% (one standard deviation) of the linearity index. We also measured dose-rate responses by placing the coatings at surface, with SSD ranging from 70 to 105 cm with 600 MU/min (FF mode), field size of 100 × 100 mm^2 and 100 MU.

Square field sizes ranged from 6 × 6 mm^2 to 100 × 100 mm^2 and relative doses were calculated with coatings irradiated with 100 MU at d_{max}. All measurements were performed at gantry 0°, SSD of 100 cm, and normalized to the 30 × 30 mm^2 field. Coatings were placed below transparent (translucence of 92%) Polymethyl Methacrylate (PMMA) plates, density of 1.19 g/cm^3, at d_{max}. Reference measurements for small fields relative responses were measured using a farmer chamber (model TW30013, PTW Dosimetry) for fields bigger than 50 × 50 mm^2 and a thimble ionization chamber (model SNC125 cc, SUN Nuclear) for smaller fields. The International Atomic Energy Agency (IAEA) publication "TRS-483: Small Field Dosimetry - Oncology Medical Physics"

Table 3
Difference of measured dose at difference depths in a 100 × 100 mm^2, 6 MV FF beam where the point optical fibre system is placed at the out-of-field of the beam (x = 60 mm), with and without the coatings.

Depth	Fibre dose without coating	Nano-01	Micro-01	Micro-02	Micro-03	Micro-04	Al_2O_3
6 MV FF							
mm	Gy	Difference (%)					
2	0.035 ± 0.001	−0.8	−1.5	−1.6	−1.8	−2.7	−2.8
4	0.031 ± 0.001	−0.8	−1.4	−1.5	−1.6	−2.8	−1.6
6	0.028 ± 0.001	−0.8	−1.2	−1.3	−1.3	−2.6	−1.8
10	0.021 ± 0.001	−0.9	−1.5	−1.6	−1.6	−2.9	−2.3
15	0.018 ± 0.001	−0.9	−1.6	−1.6	−1.8	−2.7	−2.7
20	0.017 ± 0.001	−0.9	−1.5	−1.6	−1.7	−3.00	−2.8

(Palmans et al., 2018) recommends the benchmark for reference dosimetry uncertainties of less than 2% (one standard deviation) in small fields and within 2–3% (one standard deviation) for conventional field sizes.

The capacity to check the stability of the multi-leaf collimator (MLC) and the reproducibility of the gap between leaves was studied by chair, pyramid and alternating leave QA tests (Clivio et al., 2015; Sathiyan et al., 2010; Van Esch et al., 2002). The chair field was a 100 × 100 mm^2 field containing an irregular shaped MLC forming a chair figure. The alternating leaves test was a 100 × 100 mm^2 field that had 5 mm open-closed leaves. The pyramid test had squared MLC fields of 25, 50, 75, 100, and 150 mm^2 with monitor units distributed equally between the different field sizes. Reference data was obtained using EBT3 films (Niroomand-Rad et al., 2020). These films were scanned 3 days post irradiation with an Epson 11000XL scanner (Epson, Japan) at 150 dpi resolution. QA checks were planned using the Varian Eclipse v13.6 (Varian Medical Systems Inc., Palo Alto, CA) treatment planning system (TPS) using a dosegrid of 1 mm.

3. Results

3.1. Film perturbation

Table 2 presents the difference between the doses measured with the optical fibre system at different depths, at isocentre, with and without the presence of the coatings on the surface. Starting at d_{max} position (16 mm for FF and 18 mm for FFF), the measurements resulted in a negligible average perturbation effect (~0.25%), with a maximum measured difference of −0.3 %, at depth of 100 mm of the surface for the Nano-01

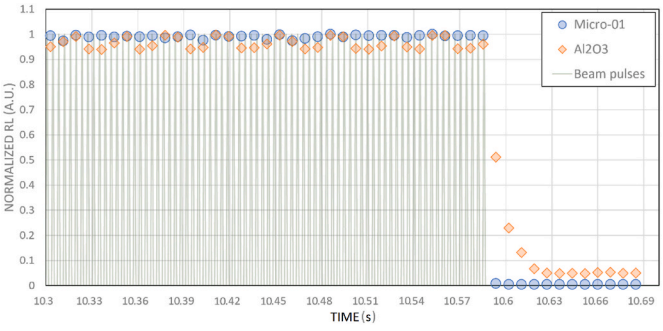

Fig. 3. Normalized RL counts (to the maximum value) versus time for both Micro-01 and Al_2O_3 coatings.

Table 4
Average of background before and after beam on, for Micro-01 and Al_2O_3, and the calculated difference (%).

Coating	Average background before beam on	Average background after beam on	Difference (%)
Micro-01	$(4.30 \pm 0.02)*10^{-3}$	$(4.32 \pm 0.01)*10^{-3}$	0.4
Al_2O_3	$(7.6 \pm 0.1)*10^{-2}$	$(7.5 \pm 0.1)*10^{-2}$	−1.3

coating. The methodology to estimate the uncertainties in the fibre dosimetry system was measured by irradiating three times the same fibre placed at the same position, and calculating the standard deviation of the readings.

Likewise, for out-of-field measurements (Table 3), the difference between the depth dose curves (without and with coatings) was <1 % for depths between 2 and 20 mm for the Nano-01. These results showed that the presence of the film interferes minimally with the measurements from the optical fibre system placed at various depths.

3.2. Afterglow

Fig. 3 presents the normalized RL counts versus time during and after irradiation for the Micro-01 and the Al_2O_3 coatings. The beam is turned off and the signal from the Al_2O_3 coating curve drops to background, within 30 ms, while the Micro-01 does not have an evident afterglow or effect of the material decay time. One can observe that the decays are within the decay times of each material. Table 4 shows that the background before and after irradiation is ≈ 0.4%, for Micro-01 and ≈-1.3%, for Al_2O_3.

3.3. Dose-rate response

The measured pixel light intensity from squared fields increased with dose-rate for all the $(C_{44}H_{38}P_2)MnCl_4$ coatings, being the 0.05 Gy/min and 4 Gy/min the dullest and 6 Gy/min and 14 Gy/min the brightest images for FF and FFF, respectively. The system's dose rate response (Fig. 4), translated from pixel light intensities, resulted in linear lines ($R^2 > 0.999$), with upper plots showing good linearity index for the whole range of dose-rates, where the ±2% deviation (indicated with light blue areas) indicate better agreement for $(C_{44}H_{38}P_2)MnCl_4$ coatings compared to the Al_2O_3:C,Mg coating, although none of the plots present saturation or deviation from linearity along the studied dose rates.

The six curves are very similar, with the pixel intensities increasing linearly with dose-rate even in the transition between FF and FFF modes. The standard deviation (1 SD), not plotted in the graphs, are below 1% (for the dose rates ≥1 Gy/min) and below 2% (for the dose rates <1 Gy/min).

The delta RL from all coatings, placed at the surface, varying the SSD (70–105 cm) in FF mode is shown in Fig. 5. In all plots, the curves are very similar, with the pixel intensities decreasing with the power law fitting curves close to x^{-2}. Deviations are possibly due to the errors in positioning.

We integrated the data obtained with the Nano-01 coating, so that dose response curves were determined using data measured with different dose rates. We have chosen this coating because it is the one with the lowest light yield, due to the composition of the coating (nano particles). The chosen integration time was t = 20 ms. Fig. 6 shows that no difference is observed for these dose response curves, using integrated dose rates from 0.05 to 14 Gy/min. In Table 5 the delivered dose per beam pulse is indicated for each mode (FF or FFF) for the lowest dose rate. This gives an indication of the system capability to measure not only the lowest dose rates available in the machine, but also the lowest doses. Conventional LINACs have photons pulses on the order of 3 μs, that are pulsed in different repetition frequencies to change the delivered machine "dose rate". In the lowest dose-rates, the camera + coating system is capable of assessing the machine pulses individually.

3.4. Small field relative doses

Shown in Fig. 7a is an examples of crossline square fields measured with the Nano-01 coating (upper plot), for fields of 30 × 30, 20 × 20, 10 × 10, 8 × 8 and 6 × 6 mm^2. The boundaries of the fields can be clearly seen for all the fields. The real time image (Fig. 7a, lower image) from the Nano-01 coating irradiated with 10 × 10 mm^2 field indicates sharp field edges and reasonable uniformity. The data presented in Fig. 7b, for all the coatings, clearly indicates the impact of crystal sizes on the relative doses calculated for the smallest field sizes. The relative difference of these measurements indicated in the upper plot, shows that the Nano-01 has differences <2% along all the field sizes (light blue area, showing ± 2% deviations). It is noteworthy that a good agreement was obtained for the relative doses from all the coatings for field sizes above 20 × 20 mm^2.

The largest differences were observed for the Al2O3, with largest differences almost reaching 22% for the smallest field size. In all the coatings types, the relative doses presents a constant decrease with respect to the largest field size (100 × 100 mm^2). Standard deviations are smaller than the symbols and not plotted.

3.5. QA alternating leaves test

Because the Nano-01 coating has so far presented the most favorable dosimetric characteristics, in special for relative dose in various field sizes, the QA results are presented in respect to this coating alone. All features from the alternating leave test are observed by the image presented in Fig. 8a such as the characteristic peaks and valleys, equally spaced in an area of 100 × 100 mm^2.

The differences in the valleys between EBT3 film and Nano-01 coating (Fig. 8b) presented very similar full width at half maximum (FWHM) for the all the inner leaves (Table 6), with larger deviations being observed for the two outer leaves (≈3.5%).

3.6. QA pyramid test

The superposition of squared profiles acquired with the Nano-01 coating provided a pyramid-like light distribution image (Fig. 9a). The film's pixel intensities (normalized to the maximum value) against length was compared with the profile from the measured pyramid acquired with the EBT3 (yellow line from Fig. 9a, plotted in Fig. 9b). The curves increased smoothly with length to reach the maximum value around 69 mm, decreasing in a mirrored way to reach a minimum at 110 mm. The differences between both curves were mostly within ±3% for the interval 20–90 mm, with larger deviations at both extremities.

3.7. QA chair test

The real time image acquired from the planned chair test (Fig. 10) outlined different profiles along the crossline and inline fields that correctly resembled a chair. To quantify the accuracy of the image, we chose two crossing lines from the chair image (line 1 and 2, Fig. 10) and plotted (Fig. 11a and b), the film's pixel intensities (normalized to the maximum value) against length (mm), compared to the same lines from the EBT3. The calculated FWHMs are very similar (<1%) (Table 7).

4. Discussion

We have successfully demonstrated the improvement of using $(C_{44}H_{38}P_2)MnCl_4$ coatings instead of Al_2O_3:C and Al_2O_3:C,Mg for real-time 2D dosimetry in conventional radiotherapy. Real-time beam tracking offers several advantages, for example, the ability to monitor beam position and shapes during treatment delivery. The key findings of

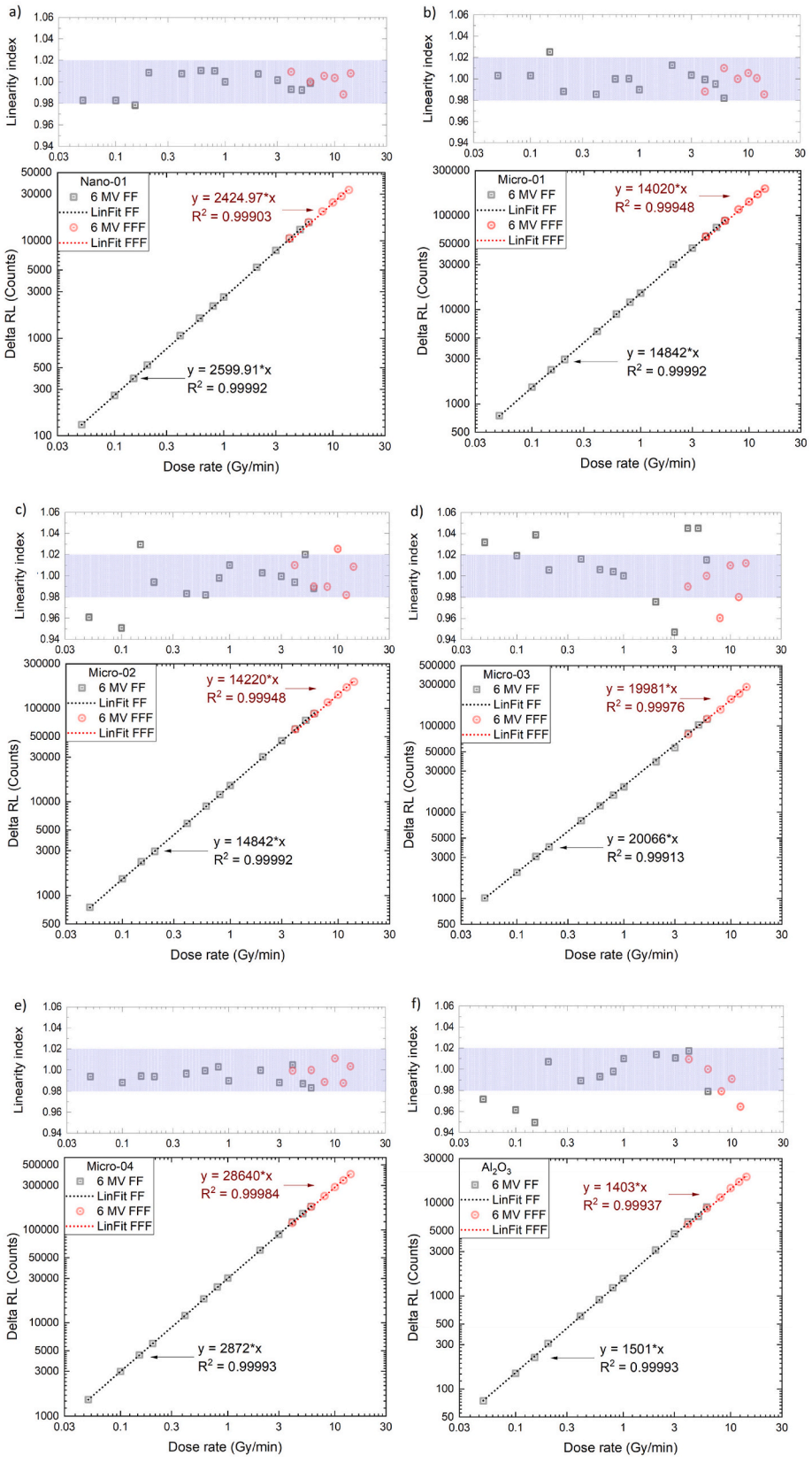

Fig. 4. Plotted delta RL measurements against LINAC dose rates for FF and FFF modes, from 0.05 to 6 Gy/min present a linear fit with a R^2 coefficient of Determination (COD) > 0.999 for a) Nano-01, b) Micro-01, c) Micro-02, d) Micro-03, e) Micro-04 and f) Al_2O_3 coatings. Upper plots show the "linearity index" relative to 1 Gy/min for each coating and the light blue area represents a deviation of ±2%.

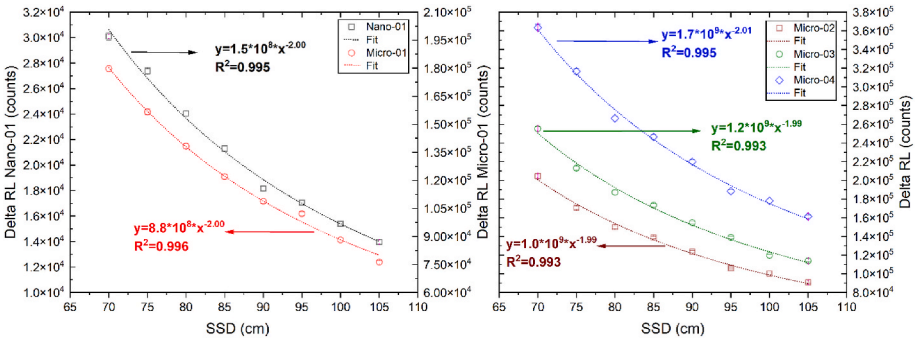

Fig. 5. Dose rate dependence for a) Nano-01, Micro-01, b) Micro-02, Micro-03 and Micro-04 coatings irradiated with 100 MU by changing the source-surface distance (SSD). Error bars (standard deviation) are plotted, but smaller than the size of the symbols.

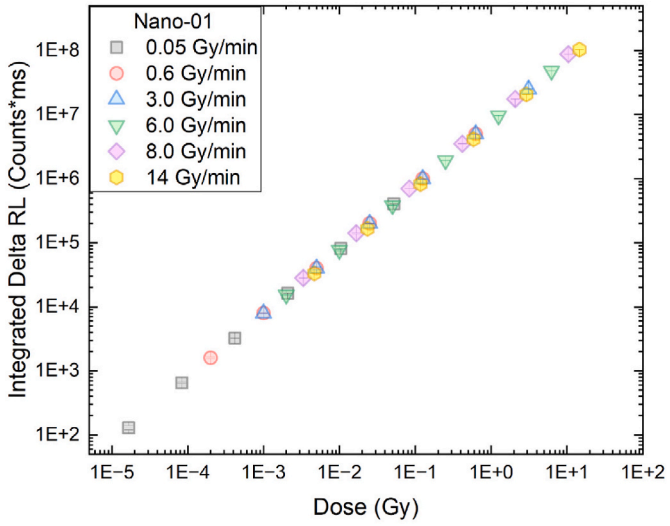

Fig. 6. Dose response curves for integrated signals using different machine dose rates (from 0.05 to 14 Gy/min). Error bars (standard deviation) are plotted, but are smaller than the symbols.

Table 5
LINAC dose per beam pulse for FF and FFF lowest possible dose rate(Xiao et al., 2015).

Energy (MV)	Min dose rate (Gy/min)	Dose per beam pulse (mGy/pulse)
6 FF	0.05	0.28
6 FFF	4.00	0.65

the study were: (a) the depth dose curves measured with and without the presence of the coatings did not present a significant beam perturbance; (b) the dose-rate response was linear for FF and FFF modes, from 0.05 to 14 Gy/min; c) measured relative dose vs field sizes showed potential for small field dosimetry for the Nano-01 coating; d) measured QA checks were reasonably consistent with EBT3 films, for the Nano-01 coating.

The $(C_{44}H_{38}P_2)MnCl_4$ coatings in the current manuscript and the Al_2O_3:C coatings from our previous work (Nascimento, 2015) did not perturb the main beam, as the difference between the curves was within the uncertainty of the optical fibre system. These results are comparable with the perturbation measured with transmission detectors (MagicPlate and monolithic silicon detector) (Alrowaili et al., 2017; Utitsarn et al., 2017), and other similar systems, such as the GOS scintillator film (−0.6%) (Jenkins et al., 2015).

For all the $(C_{44}H_{38}P_2)MnCl_4$ coatings, the measured pixel intensities increase linearly with dose-rate up to 6 Gy/min (FF mode), and 14 Gy/min (FFF mode). When measuring the coatings at difference SSDs, we observed a trend that closely fits to a x^{-2} function. We were able to measure the single pulses for the lowest dose-rates, due to shorter decay pulses compared to Al_2O_3:C (Table 1) showing the potential to measure integrated absorbed doses as low as 0.28 mGy. We did not observe any trend indicating overresponse or saturation. Ultra high dose rate (UHDR) radiation therapy, also known as FLASH radiotherapy, has recently gained large attention in the radiation oncology community. Pre-clinical data with electrons and protons UHDR beams has shown lower normal tissue radiotoxicity and increased differential response between healthy and tumor tissue (Favaudon et al., 2014). We are currently validating the $(C_{44}H_{38}P_2)MnCl_4$ coatings in an electron UHDR beam, following our recent work using these phosphor coupled to a PMMA optical fibre (Vanreusel et al., 2022), as our results do not indicate saturation at such high dose-rates (from 40 Gy/s to 1000 Gy/s).

One of the challenges encountered in quality assurance (QA) lies within dosimetry for small field sizes, utilized, for instance, in stereotactic body radiotherapy (SBRT) and in radiotherapy machines using mini and micro Multileaf Collimators (Bortfeld et al., 1999; Fürweger et al., 2016). These scenarios involve diverse factors such as varying amounts of primary and secondary scattered photons, steep gradients within the radiation field, the volume averaging effect, the absence of charged particle equilibrium, partial occlusion of the radiation source, and beam misalignment (Das et al., 2021; Lam et al., 2021). According to the IAEA 483 Code of Practice for small field dosimetry (Huq et al., 2018), detectors suitable for small field dosimetry should exhibit minimal or no energy dependence in their response to accurately measure profiles and field output factors. While many institutions utilize point detectors like ion chambers and diodes, these methods introduce uncertainties in reproducibility and positioning, which can be addressed by employing 2D detectors. Although our proposed system has not been developed to measure output factors in reference conditions, assessing the impact of coating's crystal size vs field size is an important parameter when one wants to use these coatings in surface/exit dose QA checks. The acceptance limit of ±3% of difference between expected and measured relative dose factors, at nominal beam energy of 6 MV (Lechner et al., 2018), was achieved by the Nano-01 coating for all the field sizes and for the Micro-01 coating for field sizes $\geq 8 \times 8$ mm^2.

While the Bragg-Gray cavity theory (Ma and Nahum, 1991) describes the relationship between cavity dose and surrounding medium dose, it assumes minimal interaction between adjacent cavities. This theory breaks down when grain size approaches the range of electrons, as their energy can be deposited across multiple grains. One of our previous works has addressed this limitation by using Monte Carlo (MC) simulations to consider grain size and also model the complex dynamics of energy transfer between grains in coatings using BaFBr:Eu^{2+} phosphors. This approach provided a more comprehensive prediction of energy deposition within individual phosphor particles, even at the nanoscale. We concluded that the dynamic interplay of energy transfer among crystals, in the nano and microscopic level, is a better description of the energy dependence of a composite solid state detector than the common

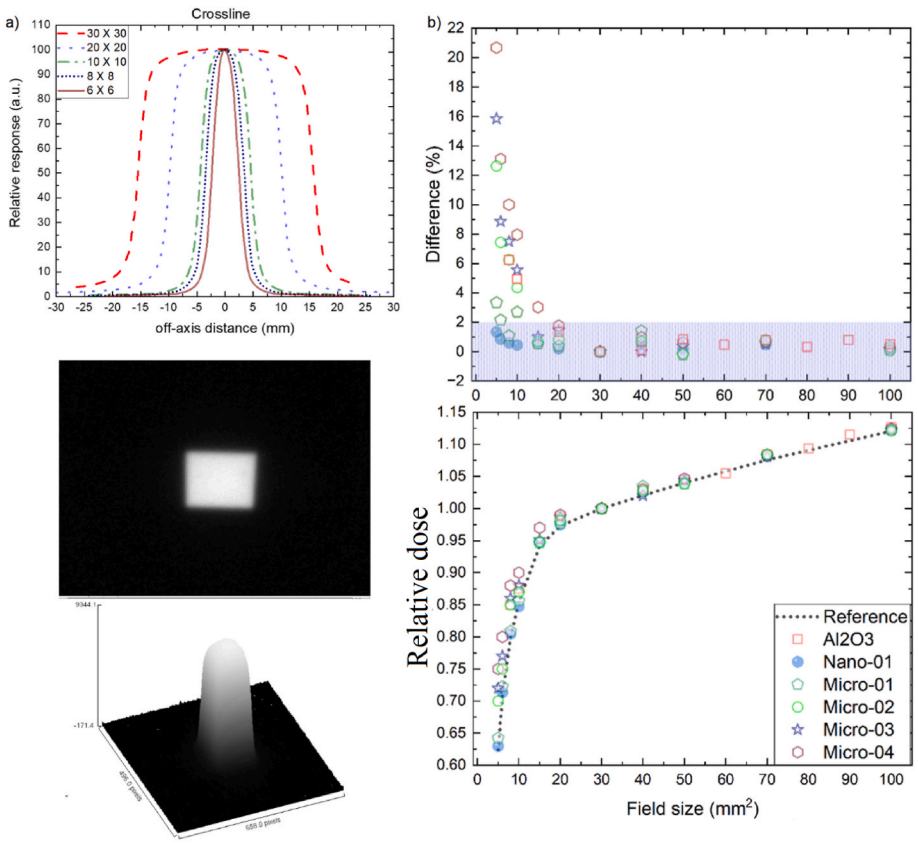

Fig. 7. a) Example of crossline profiles from the Nano-01 coating, together with measured squared field of 10 × 10 mm^2, b) relative dose vs field size calculated for all the coatings, with the difference presented in the upper plot. Error bars (standard deviation) are not presented in the plot and are smaller than the symbols.

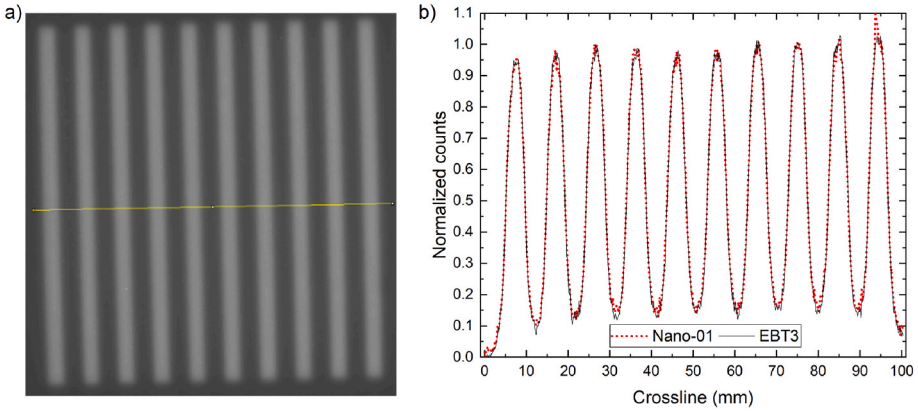

Fig. 8. Alternating leaves of 5 mm in a 100 × 100 mm^2 field detected by the (a) Nano-01 coating and (b) the normalized profile along the centre of the image (yellow line crossing the image) in comparison with the profile obtained with the EBT3 film. Error bars (standard deviation) are not presented in the plot and are smaller than the symbols.

use of theoretical Z_{eff}, and that smaller crystal sizes results in improved energy dependence (De Saint-Hubert et al., 2024b).

We have applied a similar method, using MC simulations in the response of our $(C_{44}H_{38}P_2)MnCl_4$ coatings for mono-energetic x-rays. The simulations demonstrated, for an x-ray energy of 25 keV, that the dose response to water normalized to Co-60, reduced from 6 to 1.3 when comparing a coating with a grain size of 75 μm to one with 0.23 μm. It is worth noting that we were not able to provide a detailed response of crystal size vs small field sizes in conventional radiotherapeutic beams due to the challenges in modelling the LINAC and all beam modifiers, which was beyond the scope of the current work. Still our experimental data were able to demonstrate that a reduced grain size can be more optimal for small field dosimetry as it can reduce the energy dependence, as was already shown in a previous study (De Saint-Hubert et al., 2024b).

Previous works using coatings based on Al_2O_3:C or Al_2O_3:C,Mg presented good results as a real time 2D detector using clinical beams. However, for small delivered fields (<5 mm) in the alternating leave test, the differences in the valleys between TPS and Al_2O_3:C coating presented an average deviation of 12%, with maximum and minimum differences of 15% and 5%. The FWHM for the planned (TPS) was 4.9 mm, while the Al_2O_3:C presented an average of 6.7 ± 0.2 mm (Nascimento et al., 2020). A similar issue with lower resolution was also reported for 2D planar and cylindrical diode arrays (Woon et al., 2018),

Table 6
Calculated FWHM from EBT3 and Nano-01 and their difference.

FWHM (mm)		%
EBT3	Nano-01	
4.72	4.39 ± 0.04	3.62
4.23	4.25 ± 0.02	0.24
4.55	4.57 ± 0.01	0.22
4.50	4.61 ± 0.01	1.21
4.52	4.55 ± 0.02	0.33
4.45	4.50 ± 0.01	0.56
4.52	4.55 ± 0.03	0.33
4.45	4.50 ± 0.01	0.56
4.51	4.45 ± 0.03	0.67
4.71	4.40 ± 0.04	3.40

while other studies presented discrepancies of 20–40% between Monte Carlo simulations, TPS and measurements (Bergman et al., 2014; Paganini et al., 2019). Part of the overresponse observed for Al_2O_3:C coatings in the QA tests in our previous work and relative dose vs field size presented in Fig. 7 were due to the films material's specific energy dependency for energies below 100 keV (Gasparian et al., 2012; Tariq et al., 2019). For the $(C_{44}H_{38}P_2)MnCl_4$ coatings, we have observed good agreements for the alternating leaves, pyramid and chair QA tests. Measured profiles were comparable with those obtained with the EBT3 film within 1.5% when comparing FWHM values.

Our study gives additional evidence that one important parameter to optimize the energy dependence of luminescence materials is the grain size of composites. By reducing the grain size from micro to nano sizes, we have demonstrated the reduced impact in, for example, relative doses in small fields, which also translates in the QA tests where alternating leaves of 5 mm could be measured with the coating with the smallest grain size (Nano-01). This result is in line with previous studies (Cunha et al., 2017; De Saint-Hubert et al., 2024b; Kalyvas and Liaparinos, 2014; Nascimento et al., 2022), where similar improvements in energy dependence were observed.

We are currently extending the characterization of the nano $(C_{44}H_{38}P_2)MnCl_4$ coating under various beam conditions, including different energies (X-rays, electron-Flash, proton and carbon beams), to further explore its potential for a wider range of clinical applications in radiotherapy.

5. Conclusion

The measurements reported in this work present the potential of $(C_{44}H_{38}P_2)MnCl_4$ RL coatings for clinical dosimetry in a wide range of tests including basic dosimetric characterization and machine QA. We compared these coatings regarding their dose-rate response and relative doses measured in small fields. The coating with most favorable outcome was further tested in three different machine QA tests. In conclusion, we have presented data of a prototype system with potential for ensuring the accurate and safe delivery of radiation in clinical practice. This study differed from our previous work by replacing the coating type (Al_2O_3:C to $(C_{44}H_{38}P_2)MnCl_4$ RL) and by demonstrating their dosimetric improvement by decreasing the crystal sizes. Future work will focus on assessing more clinical relevant scenarios, with patient plans, where the dynamic deposition of dose will be assessed.

CRediT authorship contribution statement

Luana de Freitas Nascimento: Writing – original draft, Validation, Project administration, Methodology, Investigation, Funding acquisition, Formal analysis, Data curation, Conceptualization. **Marijke De Saint-Hubert:** Writing – review & editing. **Wouter Crijns:** Writing – review & editing. **Marco Caprioli:** Writing – review & editing. **Laurence Delombaerde:** Writing – review & editing. **Dirk Vandenbroucke:** Writing – review & editing. **Paul Leblans:** Writing – review & editing, Conceptualization. **Katleen Himschoot:** Investigation, Writing - review & editing. **Paul Sterckx:** Resources. **Jo Goossens:** Writing – review & editing. **Verdi Vanreusel:** Writing – review & editing, Resources. **Dirk Verellen:** Writing – review & editing.

Declaration of competing interest

The authors declare that they have no known competing financial interests or personal relationships that could have appeared to influence the work reported in this article.

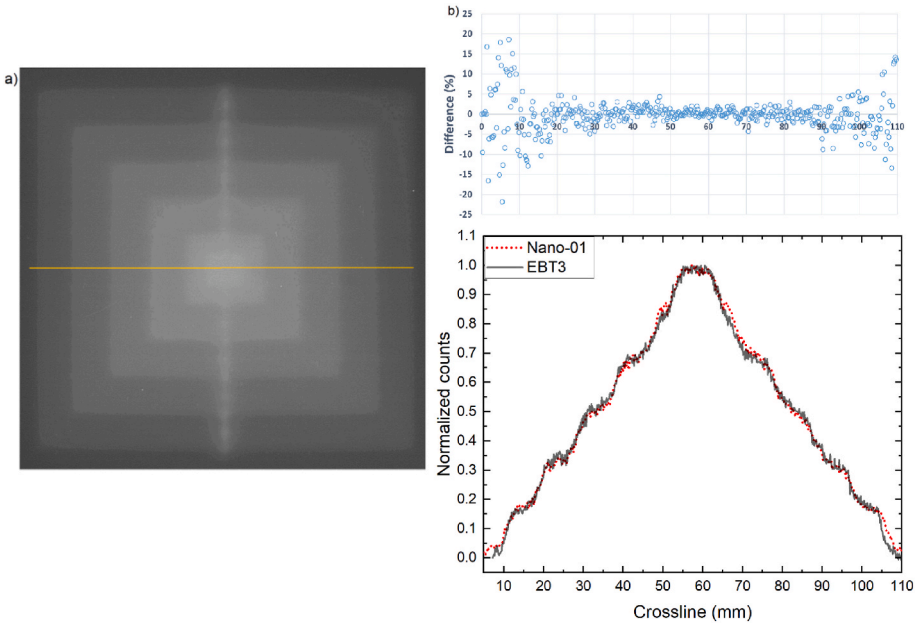

Fig. 9. Pyramid test a) captured by the Nano-01 coatings, with the superposition of various square field sizes and b) profile comparison with EBT3 for the yellow line. Upper plot is the difference between the EBT3 film and the Nano-01 coating. Error bars (standard deviation) are not presented in the plot and are smaller than the symbols.

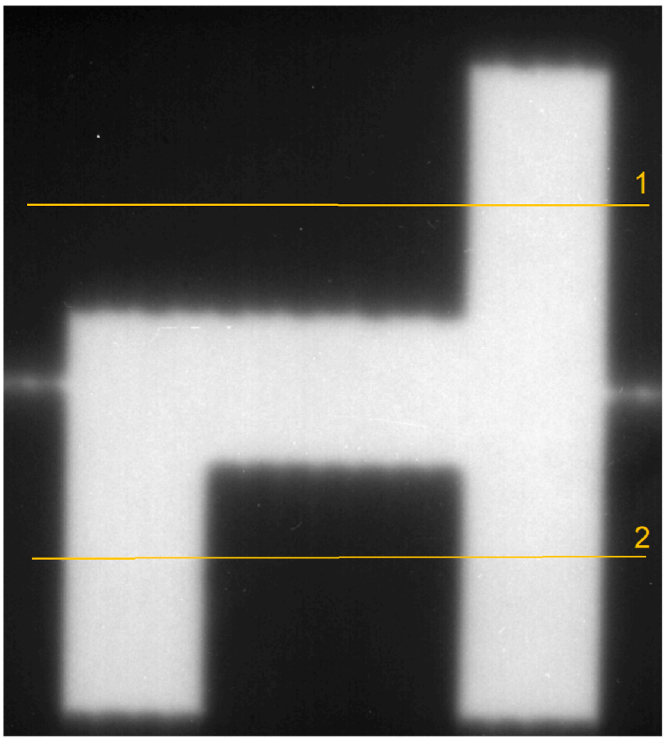

Fig. 10. Chair test in a 100 × 100 mm^2 field captured by the Nano-01 coating with specific profiles (lines 1 and 2).

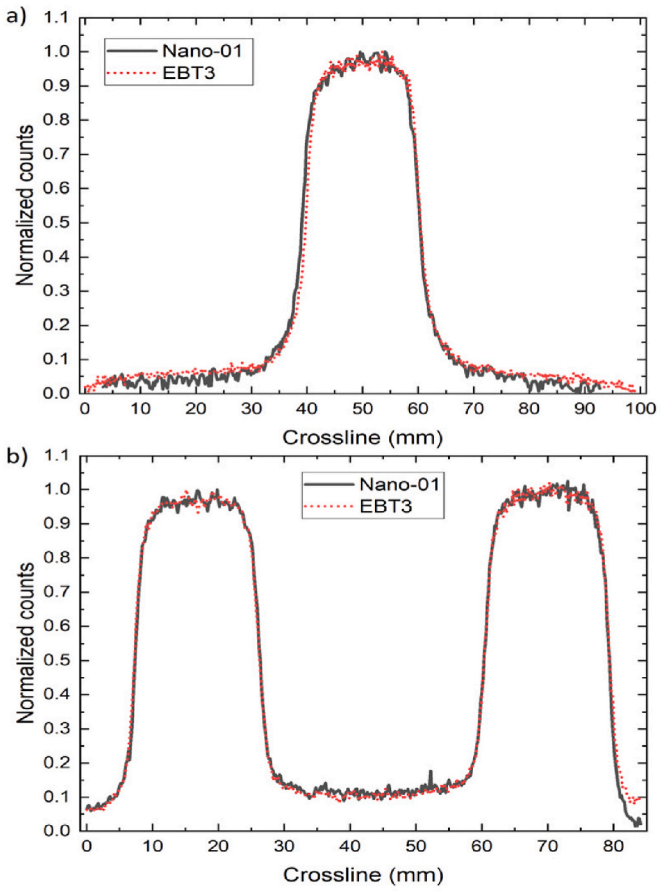

Fig. 11. Profile comparison of Nano-01 with EBT3 for a) line 1 and b) line 2. Error bars are not presented in the plot and are smaller than the symbols.

Table 7
Calculated FWHM from EBT3 and Nano-01 and their difference.

Line	FWHM (mm)		%
	EBT3	Nano-01	
1	4.72	4.61 ± 0.03	0.62
2	4.23	4.25 ± 0.03	0.24
	4.55	4.57 ± 0.02	0.22

Data availability

Data will be made available on request.

Acknowledgement

Luana de Freitas Nascimento has received a travel grant from the Fonds voor Wetenschappelijk Onderzoek (FWO, Belgium) to attend the Solid State Dosimetry (SSD20) conference with reference number K1D4623N. This work has been supported by a Flanders Innovation and Entrepreneurship VLAIO, Belgium) research grant named QUARTEL (HBC 2020 3003).

References

Aboelezz, E., Pogue, B.W., 2023. Review of nanomaterial advances for ionizing radiation dosimetry. Appl. Phys. Rev. 10.
AGFA, 2024. SYNAPS Synthetic Paper 115. https://www.agfa.com/specialty-products/solutions/synaps-synthetic-paper/.
Akselrod, M.S., Akselrod, A.E., 2006. New Al2O3: C, Mg crystals for radiophotoluminescent dosimetry and optical imaging. Radiat. Protect. Dosim. 119, 218–221.
Almond, P.R., Biggs, P.J., Coursey, B.M., Hanson, W.F., Huq, M.S., Nath, R., Rogers, D. W., 1999. AAPM's TG-51 protocol for clinical reference dosimetry of high-energy photon and electron beams. Med. Phys. 26, 1847–1870.
Alrowaili, Z., Lerch, M., Petasecca, M., Carolan, M., Rosenfeld, A., 2017. Effect of scattered electrons on the 'Magic Plate' transmission array detector response. J. Phys. Conf., 012033. IOP Publishing.
Andreo, P., Huq, M.S., Westermark, M., Song, H., Tilikidis, A., DeWerd, L., Shortt, K., 2002. Protocols for the dosimetry of high-energy photon and electron beams: a comparison of the IAEA TRS-398 and previous international Codes of Practice. Phys. Med. Biol. 47, 3033.
Attix, F.H., 2008. Introduction to Radiological Physics and Radiation Dosimetry. John Wiley & Sons.
Basler, 2024. Pylon camera software suite. Document number: AW001406 Version: 84 ed. Basler. https://docs.baslerweb.com/pylon-camera-software-suite.
Beaulieu, L., Beddar, S., 2016. Review of plastic and liquid scintillation dosimetry for photon, electron, and proton therapy. Phys. Med. Biol. 61, R305.
Beddar, S., Beaulieu, L., 2016. Scintillation Dosimetry. CRC Press.
Bergman, A.M., Gete, E., Duzenli, C., Teke, T., 2014. Monte Carlo modeling of HD120 multileaf collimator on Varian TrueBeam linear accelerator for verification of 6X and 6X FFF VMAT SABR treatment plans. J. Appl. Clin. Med. Phys. 15, 148–163.
Bhadane, M.S., Gavhane, K., Kulkarni, P.P., Dahiwale, S., Bhoraskar, V., More, M., Patil, P., Dhole, S., 2020. Particle size dependent TL response of CaF2: Dy phosphor for gamma dosimetry. J. Lumin. 223, 117168.
Borca, V.C., Pasquino, M., Russo, G., Grosso, P., Cante, D., Sciacero, P., Girelli, G., Porta, M.R.L., Tofani, S., 2013. Dosimetric characterization and use of GAFCHROMIC EBT3 film for IMRT dose verification. J. Appl. Clin. Med. Phys. 14, 158–171.
Bortfeld, T., Schlegel, W., Hoever, K., Schulz-Ertner, D., 1999. Mini and micro multileaf collimators. Med. Phys 26, 1094.
Bresciani, S., Poli, M., Miranti, A., Maggio, A., Di Dia, A., Bracco, C., Gabriele, P., Stasi, M., 2018. Comparison of two different EPID-based solutions performing pretreatment quality assurance: 2D portal dosimetry versus 3D forward projection method. Phys. Med. 52, 65–71.
Clivio, A., Vanetti, E., Rose, S., Nicolini, G., Belosi, M.F., Cozzi, L., Baltes, C., Fogliata, A., 2015. Evaluation of the machine performance check application for TrueBeam Linac. Radiat. Oncol. 10, 1–11.
Cunha, M., Testa, E., Beuve, M., Balosso, J., Chaikh, A., 2017. Considerations on the miniaturization of detectors for in vivo dosimetry in radiotherapy: a Monte Carlo study. Nucl. Instrum. Methods Phys. Res. Sect. B Beam Interact. Mater. Atoms 399, 20–27.
Das, I.J., Francescon, P., Moran, J.M., Ahnesjö, A., Aspradakis, M.M., Cheng, C.W., Ding, G.X., Fenwick, J.D., Saiful Huq, M., Oldham, M., 2021. Report of AAPM Task Group 155: megavoltage photon beam dosimetry in small fields and non-equilibrium conditions. Med. Phys. 48, e886–e921.
de Freitas Nascimento, L., Leblans, P., van der Heyden, B., Akselrod, M., Goossens, J., Correa Rocha, L.E., Vaniqui, A., Verellen, D., 2022. Characterisation and quenching correction for an Al2O3: C optical fibre real time system in therapeutic proton, helium, and carbon-charged beams. Sensors 22, 9178.

De Saint-Hubert, L., Caprioli, M., de Freitas Nascimento, L., Delombaerde, L., Himschoot, K., Vandenbroucke, D., Leblans, P., Crijns, W., 2024a. New optically stimulated luminescence dosimetry film optimized for energy dependence guided by Monte Carlo simulations. Phys. Med. Biol. (in press).
De Saint-Hubert, M., Caprioli, M., de Freitas Nascimento, L., Delombaerde, L., Himschoot, K., Vandenbroucke, D.A., Leblans, P., Crijns, W., 2024b. New optically stimulated luminescence dosimetry film optimized for energy dependence guided by Monte Carlo simulations. Phys. Med. Biol.
Favaudon, V., Caplier, L., Monceau, V., Pouzoulet, F., Sayarath, M., Fouillade, C., Poupon, M.-F., Brito, I., Hupé, P., Bourhis, J., 2014. Ultrahigh dose-rate FLASH irradiation increases the differential response between normal and tumor tissue in mice. Sci. Transl. Med. 6, 245ra293-245ra293.
Fürweger, C., Prins, P., Coskan, H., Heijmen, B.J., 2016. Characteristics and performance of the first commercial multileaf collimator for a robotic radiosurgery system. Med. Phys. 43, 2063–2071.
Galavis, P.E., Hu, L., Holmes, S., Das, I.J., 2019. Characterization of the plastic scintillation detector Exradin W2 for small field dosimetry. Med. Phys. 46, 2468–2476.
Gasparian, P., Vanhavere, F., Yukihara, E., 2012. Evaluating the influence of experimental conditions on the photon energy response of Al2O3: C optically stimulated luminescence detectors. Radiat. Meas. 47, 243–249.
Guillot, M., Beaulieu, L., Archambault, L., Beddar, S., Gingras, L., 2011. A new water-equivalent 2D plastic scintillation detectors array for the dosimetry of megavoltage energy photon beams in radiation therapy. Med. Phys. 38, 6763–6774.
Huq, M.S., Andreo, P., Song, H., 2001. Comparison of the IAEA TRS-398 and AAPM TG-51 absorbed dose to water protocols in the dosimetry of high-energy photon and electron beams. Phys. Med. Biol. 46, 2985.
Huq, M.S., Hwang, M.S., Teo, T.P., Jang, S.Y., Heron, D.E., Lalonde, R.J., 2018. A dosimetric evaluation of the IAEA-AAPM TRS 483 code of practice for dosimetry of small static fields used in conventional linac beams and comparison with IAEA TRS-398, AAPM TG 51, and TG 51 Addendum protocols. Med. Phys. 45, 4257–4273.
Jenkins, C.H., Naczynski, D.J., Yu, S.J.S., Xing, L., 2015. Monitoring external beam radiotherapy using real-time beam visualization. Med. Phys. 42, 5–13.
Jiang, T., Ma, W., Zhang, H., Tian, Y., Lin, G., Xiao, W., Yu, X., Qiu, J., Xu, X., Yang, Y., 2021. Highly efficient and tunable emission of lead-free manganese halides toward white light-emitting diode and X-ray scintillation applications. Adv. Funct. Mater. 31, 2009973.
Kalyvas, N., Liaparinos, P., 2014. Comparing analytical and Monte Carlo optical diffusion models in phosphor-based X-ray detectors. Medical Imaging 2014: Physics of Medical Imaging 1112–1119. SPIE.
Lam, S., Bradley, D., Khandaker, M.U., 2021. Small-field radiotherapy photon beam output evaluation: detectors reviewed. Radiat. Phys. Chem. 178, 108950.
Lechner, W., Wesolowska, P., Azangwe, G., Arib, M., Alves, V.G.L., Suming, L., Ekendahl, D., Bulski, W., Samper, J.L.A., Vinatha, S.P., 2018. A multinational audit of small field output factors calculated by treatment planning systems used in radiotherapy. Physics and Imaging in Radiation Oncology 5, 58–63.
Lian, L., Wang, X., Zhang, P., Zhu, J., Zhang, X., Gao, J., Wang, S., Liang, G., Zhang, D., Gao, L., 2021. Highly luminescent zero-dimensional organic copper halides for X-ray scintillation. J. Phys. Chem. Lett. 12, 6919–6926.
Ma, C.-m., Nahum, A., 1991. Bragg-Gray theory and ion chamber dosimetry for photon beams. Phys. Med. Biol. 36, 413.
Mijnheer, B., 2019. EPIDs and QA of advanced treatments. J. Phys. Conf., 012061. IOP Publishing.
Nascimento, L., Leblans, P., van der Heyden, B., Akselrod, M., Goossens, J., Verellen, D., Kodaira, S., 2022. Characterization and quenching correction for a 2D real time radioluminescent system in therapeutic proton and carbon charged beams. Sensor Actuator Phys. 345, 113781.
Nascimento, L., Vanhavere, F., Kodaira, S., Kitamura, H., Verellen, D., De Deene, Y., 2015. Application of Al 2 O 3: C+ fibre dosimeters for 290MeV/n carbon therapeutic beam dosimetry. Radiat. Phys. Chem. 115, 75–80.
Nascimento, L., Veronese, I., Loi, G., Mones, E., Vanhavere, F., Verellen, D., 2018. Radioluminescence results from an Al2O3: C fiber prototype: 6 MV medical beam. Sensor Actuator Phys. 274, 1–9.
Nascimento, L.d.F., 2015. On-line dosimetry for radiotherapy using non-invasive optical fibre sensors with Al2O3:C RL/OSL detector, Faculteit Geneeskunde en Gezondheidswetenschappen. Vakgroep Radiotherapie en experimenteel kankeronderzoek. University of Ghent, p. 169.
Nascimento, L.d.F., Goossens, J., Leblans, P., Sterckx, P., Vanhavere, F., Struelens, L., Akselrod, M., Verellen, D., 2021. Real-time two dimensional dosimetry using Al2O3: C and Al2O3: C, Mg films. Sensor Actuator Phys. 318, 112491.
Nascimento, L.F., Verellen, D., Goossens, J., Struelens, L., Vanhavere, F., Leblans, P., Akselrod, M., 2020. Two-dimensional real-time quality assurance dosimetry system using μ-Al2O3: C, Mg radioluminescence films. Physics and imaging in radiation oncology 16, 26–32.
Niroomand-Rad, A., Chiu-Tsao, S.T., Grams, M.P., Lewis, D.F., Soares, C.G., Van Battum, L.J., Das, I.J., Trichter, S., Kissick, M.W., Massillon-Jl, G., 2020. Report of AAPM task group 235 radiochromic film dosimetry: an update to TG-55. Med. Phys. 47, 5986–6025.
O'Keeffe, S., McCarthy, D., Woulfe, P., Grattan, M., Hounsell, A., Sporea, D., Mihai, L., Vata, I., Leen, G., Lewis, E., 2015. A review of recent advances in optical fibre sensors for in vivo dosimetry during radiotherapy. The British journal of radiology 88, 20140702.
Paganini, L., Reggiori, G., Stravato, A., Palumbo, V., Mancosu, P., Lobefalo, F., Gaudino, A., Fogliata, A., Scorsetti, M., Tomatis, S., 2019. MLC parameters from static fields to VMAT plans: an evaluation in a RT-dedicated MC environment (PRIMO). Radiat. Oncol. 14, 1–13.
Pagonis, V., Polymeris, G.S., Kitis, G., Sahare, P., 2023. The effect of particle size on the radiation dose response of luminescence signals from nanophosphors. Radiat. Meas. 166, 106965.
Palmans, H., Andreo, P., Huq, M.S., Seuntjens, J., Christaki, K.E., Meghzifene, A., 2018. Dosimetry of small static fields used in external photon beam radiotherapy: summary of TRS-483, the IAEA–AAPM international Code of Practice for reference and relative dose determination. Med. Phys. 45, e1123–e1145.
Rangaraj, D., Yaddanapudi, S., Cai, J., 2019. Transmission detectors are safe and the future for patient-specific QA in radiation therapy. Med. Phys. 46, 1–4.
Rodriguez, M., Denis, G., Akselrod, M., Underwood, T., Yukihara, E., 2011. Thermoluminescence, optically stimulated luminescence and radioluminescence properties of Al2O3: C, Mg. Radiat. Meas. 46, 1469–1473.
Sathiyan, S., Ravikumar, M., Varatharaj, C., Supe, S., Keshava, S., 2010. IMRT Implementation and patient specific dose verification with film and ion chamber array detectors. Gulf J Oncolog 1, 20–27.
Schindelin, J., Arganda-Carreras, I., Frise, E., Kaynig, V., Longair, M., Pietzsch, T., Preibisch, S., Rueden, C., Saalfeld, S., Schmid, B., 2012. Fiji: an open-source platform for biological-image analysis. Nat. Methods 9, 676–682.
Stevens, S., Moloney, S., Blackmore, A., Hart, C., Rixham, P., Bangiri, A., Pooler, A., Doolan, P., 2023. IPEM topical report: guidance for the clinical implementation of online treatment monitoring solutions for IMRT/VMAT. Phys. Med. Biol. 68, 18TR02.
Stralingsdosimetrie, N.C.V., 2008. Code of Practice for the Absorbed Dose Determination in High Energy Photon and Electron Beams. Rep.2008.
Tariq, M., Gomez, C., Riegel, A.C., 2019. Dosimetric impact of placement errors in optically stimulated luminescent in vivo dosimetry in radiotherapy. Physics and Imaging in Radiation Oncology 11, 63–68.
Timakova, E., Bazalova-Carter, M., Zavgorodni, S., 2023. Characterization of a 0.8 mm3 Medscint plastic scintillator detector system for small field dosimetry. Phys. Med. Biol. 68, 175040.
Utitsarn, K., Alrowaili, Z.A., Stansook, N., Petasecca, M., Carolan, M., Perevertaylo, V.L., Lerch, M., Rosenfeld, A., 2017. Impact of a monolithic silicon detector operating in transmission mode on clinical photon beams. Phys. Med. 43, 114–119.
Van Esch, A., Bohsung, J., Sorvari, P., Tenhunen, M., Paiusco, M., Iori, M., Engström, P., Nyström, H., Huyskens, D.P., 2002. Acceptance tests and quality control (QC) procedures for the clinical implementation of intensity modulated radiotherapy (IMRT) using inverse planning and the sliding window technique: experience from five radiotherapy departments. Radiother. Oncol. 65, 53–70.
Vanreusel, V., Gasparini, A., Galante, F., Mariani, G., Pacitti, M., Cociorb, M., Giammanco, A., Reniers, B., Reulens, N., Shonde, T.B., 2022. Point scintillator dosimetry in ultra-high dose rate electron "FLASH" radiation therapy: a first characterization. Phys. Med. 103, 127–137.
Veronese, I., Cantone, M., Chiodini, N., Coray, A., Fasoli, M., Lomax, A., Mones, E., Moretti, F., Vedda, A., 2010. Feasibility study for the use of cerium-doped silica fibres in proton therapy. Radiat. Meas. 45, 635–639.
Woon, W., Ravindran, P.B., Ekayanake, P., Lim, Y.Y., Khalid, J., 2018. A study on the effect of detector resolution on gamma index passing rate for VMAT and IMRT QA. J. Appl. Clin. Med. Phys. 19, 230–248.
Xiao, Y., Kry, S.F., Popple, R., Yorke, E., Papanikolaou, N., Stathakis, S., Xia, P., Huq, S., Bayouth, J., Galvin, J., 2015. Flattening filter-free accelerators: a report from the AAPM therapy emerging technology assessment work group. J. Appl. Clin. Med. Phys. 16, 12–29.
Xu, L.-J., Lin, X., He, Q., Worku, M., Ma, B., 2020. Highly efficient eco-friendly X-ray scintillators based on an organic manganese halide. Nat. Commun. 11, 4329.
Xu, T., Li, W., Zhou, Z., Li, Y., Nikl, M., Buryi, M., Zhu, J., Niu, G., Tang, J., Ren, G., 2022. 0D organic manganese (II) bromide hybrids as stable and efficient X-ray scintillator. Phys. Status Solidi Rapid Res. Lett. 16, 2200175.
Yukihara, E.G., McKeever, S.W., Akselrod, M.S., 2014. State of art: optically stimulated luminescence dosimetry–Frontiers of future research. Radiat. Meas. 71, 15–24.